# Silver Adsorption on Calcium Niobate(001) Nanosheets: Calorimetric Energies That Explain Sinter-Resistant Support

Wei Zhang, Ritesh Uppuluri, Thomas E. Mallouk, and Charles T. Campbell*
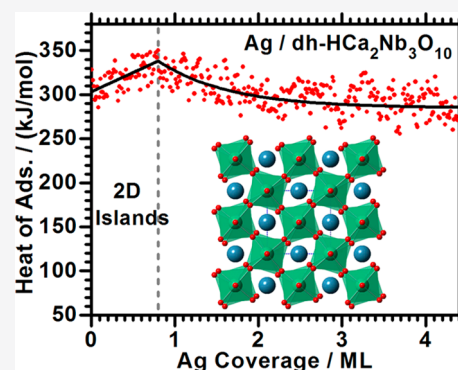
Read Online

ACCESS | 📊 Metrics & More | 📰 Article Recommendations

**ABSTRACT:** Metal nanoparticles deposited on oxide supports are essential to many technologies, including catalysts, fuel cells, and electronics. Therefore, understanding the chemical bonding strength between metal nanoparticles and oxide surfaces is of great interest. The adsorption energetics, adhesion energy, and adsorbate structure of Ag on dehydrated $HCa_2Nb_3O_{10}(001)$ nanosheets at 300 K have been studied using metal adsorption calorimetry and surface spectroscopies. These dehydrated ("dh") calcium niobate nanosheets ($dh-HCa_2Nb_3O_{10}(001)$) have the stoichiometry $Ca_4Nb_6O_{19}$. They impart unusual stability to metal nanoparticles when used as catalyst supports and are easy-to-prepare by Langmuir−Blodgett (LB) techniques, highly ordered, and essentially single-crystal surfaces of mixed oxides with a huge ratio of terrace to edge sites. Below the monolayer coverage, Ag grows on dh-$HCa_2Nb_3O_{10}(001)$ as 2D islands of thickness ~2 layers. The differential heat of Ag adsorption is initially ~303 kJ/mol, increasing slowly to ~338 kJ/mol by 0.8 ML. At higher coverages, Ag atoms mainly add on top of these 2D islands, growing 3D nanoparticles of increasing thickness, as the heat decreases asymptotically toward silver's heat of sublimation (285 kJ/mol). The adhesion energy of Ag(s) to this Ca niobate surface is estimated to be 4.33 $J/m^2$, larger than that on any oxide surface previously measured. This explains the sinter resistance reported for metal nanoparticles on this support. Electron transfer from Ag into the calcium niobate is also measured. These results demonstrate an easy way to do single-crystal-type surface science studies—and especially thermochemical measurements—on the complex surfaces of mixed oxides: using LB-deposited perovskite nanosheets and ultrahigh-vacuum annealing in $O_2$.

## 1. INTRODUCTION

Late transition metal nanoparticles supported on high area oxide surfaces are the key ingredients of many catalysts and electrocatalysts with applications to future technologies in the energy, chemical, and environmental industries. The catalytic activity and selectivity of these catalysts are strongly dependent on the size and shape of the nanoparticles, as well as on the support material.[1−5] Mixed or binary metal oxides (i.e., oxides with two metal elements) are often used as supports in catalysis with considerable improvement on various aspects of catalyst performance. The best-known example is ceria-zirconia in automotive exhaust treatment and other reactions,[6−10] but many other mixed oxides are used industrially. The presence of two metals in the oxide surely offers ample opportunities for improvement on all aspects of support chemistry, including not only the strength of bonding to metal nanoparticles but also the extent of charge transfer, lattice stress/strain control, shuttling of electrons or ions between the support and the metal as part of reaction mechanisms, etc. Thus, there is considerable motivation to understand mixed metal oxides as supports. To our knowledge, nothing is known about how the second metal in such mixed oxides influences the strength of binding of metal nanoparticles to mixed-oxide surfaces. Here

we measure for the first time how strongly metal adatoms and metal nanoparticles bond to a well-ordered mixed-oxide surface, using silver vapor adsorption calorimetry on the dehydrated $HCa_2Nb_3O_{10}(001)$ surface. The results reveal larger adsorption energies than have ever been measured for any single-metal oxide surface previously studied.

There have been many metal atom adsorption calorimetry studies on thin, single-crystal oxide films grown on thin, single-crystal metal substrates,[5,11−15] but those were all simple oxides of a single metal element. The preparation of atomically smooth single-crystal surfaces of mixed oxides (i.e., with two metal elements) in well-defined composition and a high degree of order is very seldom reported in the literature, and never on samples that would be applicable in our adsorption calorimetry because preparing such samples is very challenging. Here we

prove that we can measure adsorption energies on mixed metal oxide single crystals prepared in a simple new way that offers many exciting new possibilities for surface studies. Lamellar Nb-perovskites can be dispersed in solution as single-crystalline flat sheets that are only one layer thick but extend laterally for long distances (>1 $\mu$m).[16−20] These nanosheets can be deposited in a layer-by-layer fashion on flat substrates using Langmuir−Blodgett (LB) techniques to make thin, single-crystal mixed-oxide films.[17,18,21−24] Here, we use this method to deposit such perovskite thin films directly onto pyroelectric heat detectors, and we perform metal adsorption calorimetry on these films in a similar way as reported for spin-coated films of polymers[25] and drop-cast films of metal−organic frameworks (MOFs),[26] except that those deposited films could not be heated to high temperatures as we do here. We find that this provides excellent signal-to-noise ratio, proving that this method should be broadly applicable. This LB-film method is far easier than other methods that have been used to prepare clean single-crystal mixed-oxide surfaces and that required much more difficult sample preparations.

Perovskites, with the general formula $ABO_3$, represent probably the most studied mixed-oxide system in the field of heterogeneous catalysis. They are low-cost and easy to prepare and show a large variation in their composition and structure, allowing tailoring of their chemical and physical properties to better suit their applications.[27] Unilamellar perovskite nanosheets can be deposited in a layer-by-layer fashion on flat substrates using LB techniques to make thin and well-ordered mixed-oxide films.[18,22−24] One of the most interesting of these with respect to use as a catalyst support material, and the one we study here, is the dehydrated form of $HCa_2Nb_3O_{10}(001)$ nanosheets. This dehydrated (dh) form, which we will refer to later as $dh-HCa_2Nb_3O_{10}(001)$, actually has the stoichiometry $Ca_4Nb_6O_{19}$.[28] Each nanosheet of this material consists of three $NbO_6$ octahedral layers, with $Ca^{2+}$ in the center of the cube formed by $Nb^{5+}$ (see Figure 1), and is 1.44−1.46 nm thick (i.e., the sheet-to-sheet repeat distance in the bulk, multilayer solid structure).[28−31] These and many other perovskites can be synthesized as single- and few-layer nanosheets in solution, with lateral dimensions ranging from several hundred nanometers to a few micrometers.[16−19] The long lateral dimension indicates that these nanosheets have a huge ratio of terrace sites to sheet-edge sites, much larger than the terrace/defect site ratio on the surfaces of single crystal oxides typically studied by surface science methods in recent years. This makes them promising model surfaces with very homogeneous and well-defined surface sites for studying adsorption, for example, of metal atoms and nanoparticles if interested in their use as catalyst support materials, as we are here. These nanosheets offer an important advantage not present in normal single-crystal surfaces: they can also be prepared as powders that have a very high surface-to-volume ratio.[32−36] This means that their surface chemistry can be studied by many methods not possible on most single-crystal surfaces (e.g., volumetric adsorption, transient catalyst kinetics in normal-pressure flow reactors, etc.). It also means that they have many potential applications in real technology (e.g., as industrial catalysts or sorbents).

When used as supports for transition metal or oxide nanoparticles, powders of these $dh-HCa_2Nb_3O_{10}(001)$ nanosheets impart unusual stability against sintering to these nanoparticles[37,38] and significantly enhance their catalytic activity for water splitting.[16,39] These layered perovskites are
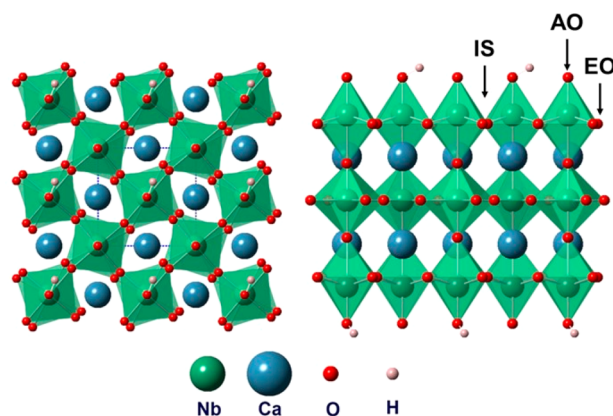


**Figure 1.** Polyhedral representations of the $HCa_2Nb_3O_{10}$ nanosheet structure, viewed from the [001] (left) and [010] (right) directions. The structure at left is the top view of the (001) surface being studied here. The dashed blue line indicates the unit cell. There are $6.74 \times 10^{14}$ O atoms/$cm^2$ on this (001) surface, half of which are in the surface OH groups. All of these H atoms, and one O atom for every two such H atoms in this structure, are removed upon dehydration to produce the dehydrated (dh) form studied here (see text). The right structure shows one complete layer of the nanosheet, which has a thickness (or repeat distance in the 3D bulk) of 1.44 nm (1.31 nm after dehydration). Labels indicate the following: AO, axial oxygen; EO, equatorial oxygen; IS, interstitial space.

also temperature-stable up to ∼825 K in powder form[28] and ∼975 K in layered-film form[40] without obvious decomposition, so they hold significant promise as support materials for later transition metal nanoparticle catalysts.

In this work, we combine surface-chemistry measurement methods developed for studying metal adsorption and nanoparticle growth on single-crystal oxide surfaces, particularly metal vapor adsorption calorimetry,[11] with this thin-film growth method for preparing much more complex perovskite mixed-oxide surfaces to investigate the adsorption of Ag atoms on $dh-HCa_2Nb_3O_{10}(001)$ nanosheet surfaces. Silver is chosen as the probe metal here because oxide-supported Ag catalysts are extensively used for selective oxidation reactions (e.g., for ethylene,[41] CO,[42] and methane[43] oxidation reactions) and show promise for a variety of other catalytic processes.[44,45] We use atomic force microscopy (AFM) to verify the lamellar sheetlike morphology of the $HCa_2Nb_3O_{10}$ nanosheet films. We report calorimetric measurements of the heat of adsorption and sticking probability of Ag atoms as a function of Ag coverage, which provide the strength of the chemical bonding interactions between Ag atoms and the $dh-HCa_2Nb_3O_{10}(001)$ surface. The results show surprisingly strong bonding between Ag and this surface, which explains the unusual stability against sintering of metal and metal oxide nanoparticles when supported on this surface that was previously reported.[37,38] We also elucidate the particle-growth mechanism and surface morphology of the evolving Ag nanoparticles using low-energy He+ ion scattering spectroscopy (LEIS). The charge transfer associated with the strong chemical reaction between the Ag atoms and the $dh-HCa_2Nb_3O_{10}$ nanosheets is also elucidated using X-ray photoelectron spectroscopy (XPS).

As far as we know, this is the first adsorption calorimetry of metal gas atoms on any atomically smooth, well-ordered mixed-oxide surface. The results demonstrate that thin LB films of layered perovskite nanosheets provide a powerful new

approach to study surface chemistry on single-crystalline mixed-oxide surfaces.

## 2. EXPERIMENTAL METHODS

The ultrahigh-vacuum (UHV) metal adsorption calorimetry apparatus, which also includes capabilities for XPS, LEIS, and metal atomic-beam surface scattering, was described previously.[25] The heat detector, the mounting of the surface to be studied, and the way it is heated have been modified as described briefly below and in more detail in another paper.[46]

Thin $LiTaO_3$ single crystals were used as pyroelectric heat detectors for adsorption calorimetry. The $LiTaO_3$ heat detectors (purchased from DIAS Infrared GmbH) were 25 $\mu$m thick crystals with 12 mm × 12 mm square shape, with both faces precoated with 100 nm thick films of a $Ni_{80}Cr_{20}$ alloy that serve as the electrodes for electrical signal measurement. When struck with a pulse of metal vapor from the atomic beam of metal atoms, these detectors generate a charge (and thus transient current through the preamplifier) in response to heat input due to the heat of metal vapor adsorption.

The $HCa_2Nb_3O_{10}(001)$ nanosheets whose surfaces we studied here were deposited directly onto these pyroelectric heat detectors by Langmuir–Blodgett methods, as will be described later. To heat these niobate nanosheets to high temperatures in order to dehydrate them (to $Ca_4Nb_6O_{19}$) and remove the hydrocarbon impurities from their surface, a new pyroelectric heat detector was required that could maintain a high pyroelectric heat-signal response after heating to high temperatures. (The heat detector used previously on this apparatus could only be heated up to ~350 K.[25,47,48]) Therefore, here we used $LiTaO_3$ single crystals as the heat detectors. $LiTaO_3$ has a Curie point of 893 K,[49] theoretically allowing samples to be heated up to ~875 K before the heat detector loses its pyroelectric response. Heating these niobate nanosheet-coated lithium tantalate crystals ("samples") in UHV required a newly designed sample platen and sample heater, which are described elsewhere.[46] Briefly, the thin samples are heated by radiation from a hot tungsten filament that is placed very near the back side of the sample. The sample is mounted on a platen such that it can be moved to different positions in the UHV chamber depending upon whether it is being studied by surface spectroscopies (XPS and LEIS) or calorimetry or is being heated for cleaning. When mounted in the calorimetry position, the platen provides electrical contacts between the electrodes on the front and back face of the sample and wires that lead outside the UHV chamber to a preamplifier.

Each heat detector was coated with four layers of $HCa_2Nb_3O_{10}(001)$ nanosheets as described earlier. Five of these samples were then mounted onto the new sample platens and stored in the sample preparation chamber with a base pressure of $2 \times 10^{-9}$ Torr. Before the experimental measurements (i.e., sticking probability, differential heat of adsorption, LEIS, and XPS), each sample was transferred to the UHV analysis chamber with a base pressure of $1 \times 10^{-9}$ mbar and heated at ~725 K for 10 min in an oxygen pressure of $2 \times 10^{-7}$ mbar to dehydrate them and remove the hydrocarbon impurities from the surface. To prevent the heat detector from cracking due to thermal expansion, the temperature was ramped up/down slowly at ~50 K/10 min. XPS spectra before and after the heating procedure for the same sample were also collected and compared to verify the removal of hydrocarbon impurities and the sample integrity (i.e., proper elemental composition not being changed by heating).

Nanosheets of $HCa_2Nb_3O_{10}(001)$ were first prepared as described previously.[37] Briefly, $KCa_2Nb_3O_{10}$ was prepared by solid-state synthesis of a stoichiometric mixture of $K_2CO_3$ (40% excess), $CaCO_3$, and $Nb_2O_5$ at 1200 °C for 12 h. The protonated form $HCa_2Nb_3O_{10} \cdot 0.5H_2O$ was obtained by acid-exchanging the potassium form ($KCa_2Nb_3O_{10}(001)$) with 1 M nitric acid for 3 days with the acid being replaced every day. The protonated form (0.1 g) was exfoliated by stirring in an aqueous solution of tetra($n$-butylammonium) (TBA) hydroxide (25 mM, 100 mL) for 1 day, and the nanosheets were decanted from the unexfoliated sheets after allowing the suspension to settle overnight. These nanosheets were deposited directly onto the pyroelectric heat detector used for adsorption calorimetry as follows. The heat detectors were first cleaned using UV-ozone and then pretreated with Al Keggin ion[50] to anchor the negatively charged nanosheets. Langmuir–Blodgett deposition was performed by drop-casting the nanosheet suspension onto a trough containing the heat detector filled with nanopure water and compressing the barriers to a surface tension of 15 mN/m. The heat detector was then lifted at a speed of 4 mm/min to ensure well-packed nanosheets. The heat detector was dipped into hydrochloric acid (0.1 mM) between each deposition to remove the surface-bound tetra-$n$-butylammonium cations, as was shown to be effective.[51]

Atomic force microscopy (AFM) images were acquired in peak-force tapping mode (Bruker Icon) using a ScanAsyst-Air probe at a set point of 1 nN to verify the packing density of the nanosheets onto the pyroelectric heat detector.

The metal vapor adsorption calorimetry procedure used here has been described previously.[25] The sample platen was placed onto a large Cu thermal reservoir that was electrically connected to a preamplifier outside the UHV chamber. A 4.15-mm-diameter collimated atomic beam of Ag gas atoms was produced by a high-temperature effusion cell containing an alumina-lined tungsten crucible filled with Ag granules purchased from Alfa Aesar with 99.9% purity. The Ag beam was chopped into 100 ms pulses containing ~0.013 ML of Ag per pulse repeating every 2 s. One monolayer (ML) is defined here as $1.38 \times 10^{15}$ atoms/cm$^2$, which is the number of Ag surface atoms per unit area on the Ag(111) surface. This Ag atomic beam was then impinged onto the dh-$HCa_2Nb_3O_{10}(001)$ surface. The heat released from the metal atom adsorption generates a transient temperature rise in the dh-$HCa_2Nb_3O_{10}$ film, which is transferred by thermal diffusion to the $LiTaO_3$ heat detector. The resulting voltage response ("signal") was calibrated by the voltage response to pulses of known energy from a stabilized He–Ne laser (632.8 nm wavelength). An average sensitivity of ~650 V/J (volts per joule of heat adsorbed by dh-$HCa_2Nb_3O_{10}$) from three experimental runs was found. The typical operating temperature of the effusion cell was 1375 K, which generates some thermal radiation that impinges on the sample surface. This radiation contribution was also measured by translating a $BaF_2$ window into the path of the Ag beam, which blocked all the Ag atoms before they impinged onto the sample but passed a known fraction (~94%) of the radiation, which was subtracted from the total measured heat. The radiation contribution typically accounts for ~65% of the total measured heat in the case of Ag adsorption onto dh-$HCa_2Nb_3O_{10}(001)$. To convert the experimentally measured internal energy changes into the standard enthalpy changes at the sample temperature (300 K), the excess translational energy of the metal gas atoms at the effusion cell temperature above that for a 300 K Maxwell–Boltzmann distribution was subtracted, and a small pressure–volume work term (RT) was added, as described elsewhere.[47]

The incident Ag beam flux was measured using a quartz crystal microbalance (QCM, Inficon). The sticking probability of Ag adsorption on dh-$HCa_2Nb_3O_{10}(001)$ was measured by a modified King–Wells method,[25,47,52] which uses a line-of-sight quadrupole mass spectrometer (QMS, UTI 100C) to measure the fraction of Ag atoms that strike the surface but do not adsorb. This nonsticking signal was calibrated by a zero-sticking reference provided by measuring the integrated desorption signal of a known amount of multilayer Ag atoms on a hot Ta foil. A −500 V bias voltage was applied between the sample and the QMS to avoid electron damage to the dh-$HCa_2Nb_3O_{10}$ nanosheets.

The UHV analysis chamber is also equipped with a hemispherical electron energy analyzer (Leybold-Heraeus EA 11/100), ion gun (Leybold-Heraeus IQE 12/38), and Mg/Al K$\alpha$ dual-anode X-ray source (VG Scienta XR3E2) for low-energy He$^+$ ion scattering spectroscopy (LEIS) and X-ray photoelectron spectroscopy (XPS). The growth of Ag on dh-$HCa_2Nb_3O_{10}(001)$ was studied by LEIS using He$^+$ ions with 1.00 keV primary energy. The sample was positioned perpendicular to the energy analyzer axis, and the ion beam was directed at 45° with respect to the surface normal. Ion

fluxes were typically 15 nA/cm$^2$, and the sample was exposed to the He$^+$ ions only during spectrum acquisition. Each deposition of Ag atoms followed previous depositions consecutively, starting with a sample that had no adsorbed Ag atoms on its surface. All XPS spectra were collected using Al K$\alpha$ ($h\upsilon$ = 1486.6 eV, 130 W) as the excitation source with detection of photoelectrons normal to the surface. Each spectrum was fitted with the product of a Gaussian and a Lorentzian function after subtraction of a Shirley baseline. The overlapping Ag 3d doublets and Nb 2p doublets were deconvoluted by fixing the peak splits of both doublets at values taken from Wagner et al.[53] The binding energy (BE) scale of the analyzer was calibrated to the expected BE of the Ag 3d$_{5/2}$ peak for Ag(s) (367.9 eV),[53] as measured here for thick (6.8 ML) Ag films. All experiments were performed at 300 K.

## 3. RESULTS AND DISCUSSION

### 3.1. Surface Structure and Morphology of HCa$_2$Nb$_3$O$_{10}$(001) Nanosheet Films.

Figure 1 shows polyhedral representations of the HCa$_2$Nb$_3$O$_{10}$ structure in the [001] and [010] directions. The structural parameters used to draw this structure are from Chen et al.[29] The HCa$_2$Nb$_3$O$_{10}$(001) surface is O/OH-terminated with H atoms on every other O atom. On the basis of the structural optimization calculations done by Janik and co-workers,[38] there are three possible surface binding sites for metal atoms, all shown in Figure 1: (1) axial oxygen (AO), (2) equatorial oxygen (EO), and (3) interstitial space (IS) between NbO$_6$ polyhedra.

We deposited four layers of HCa$_2$Nb$_3$O$_{10}$(001) nanosheets on each LiTaO$_3$ heat detector. The sheetlike morphology of deposited HCa$_2$Nb$_3$O$_{10}$ nanosheets was confirmed by the sectional analysis of AFM images (Figure 2, top). The heat detectors were well-covered with a surface coverage of >95%
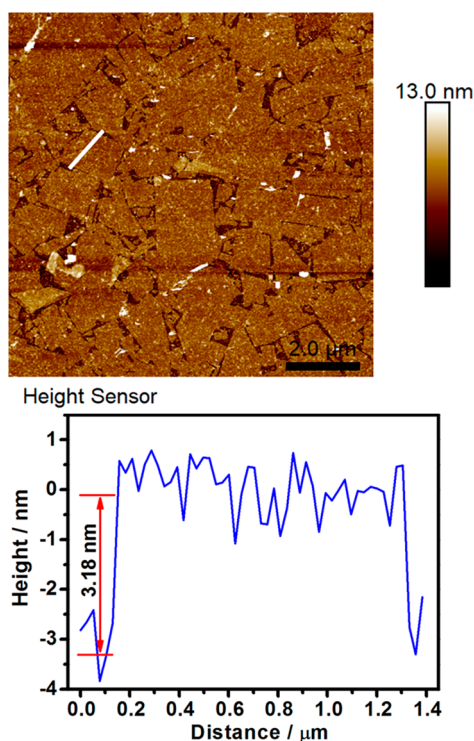


**Figure 2.** AFM image (top) of 4 layers of HCa$_2$Nb$_3$O$_{10}$(001) nanosheets deposited on a LiTaO$_3$ heat detector and height profile (bottom) across a single nanosheet along the white solid line in the image.

and negligible nanosheet overlap. The deposited nanosheets were flat with an average lateral dimension of a few microns. The thickness of individual undehydrated HCa$_2$Nb$_3$O$_{10}$ nanosheets estimated from the c-axis lattice parameter measured from crystallographic data of the bulk 3D solid is ∼1.44 nm.[28] Our AFM height profile of the as-deposited film (Figure 2 bottom) shows an overestimated thickness of 3.18 nm possibly due to (1) adsorbed H$_2$O and hydrocarbon molecules in the interlayer space, (2) increased surface roughness of individual nanosheets and multilayers of nanosheets not being perfectly packed, and/or (3) systematic errors[54] in AFM height profile measurements. The overall thicknesses of the deposited nanosheet films indicate that these films show bulklike characteristics with no or negligible film-thickness effects, which have been reported previously for metals on oxide thin films, when the oxide film thickness drops to ∼1 nm.[55−57]

### 3.2. HCa$_2$Nb$_3$O$_{10}$(001) Films before and after Heating.

These HCa$_2$Nb$_3$O$_{10}$(001) nanosheet films were cleaned and dehydrated by heating to ∼725 K in vacuum before use in studying Ag adsorption. These films are known to dehydrate upon heating at ∼575 K to form Ca$_4$Nb$_6$O$_{19}$ (i.e., 2HCa$_2$Nb$_3$O$_{10}$ → Ca$_4$Nb$_6$O$_{19}$ + H$_2$O(g)).[28] The structure is still quite similar to Figure 1,[28] but all the H is removed (from the nanosheet's surface hydroxyl groups) and one surface O atom is removed for every two such H atoms. The Nb bonds to the lost O atom are replaced by Nb bonds to a surface O atom of the neighboring nanosheet, thereby linking together the parallel nanosheets (see Figure 5 in ref 28). This decreases the c-axis lattice parameter (nanosheet-to-nanosheet separation) slightly to ∼1.31 nm.[28] We refer to this dehydrated form as dh-HCa$_2$Nb$_3$O$_{10}$(001) below. To produce this dehydrated calcium niobate, each sample was heated to ∼725 K at a rate of 50 K/10 min in an O$_2$ pressure of 2 × 10$^{-7}$ mbar and held there for 10 min. The sample was then cooled with the same rate in the same O$_2$ pressure. The heating/cooling rates were slow because faster rates sometimes caused the LiTaO$_3$ crystals to crack.

Figure 3 shows XPS spectra measured before and after the heating procedure for the 4-layer-thick nanosheet films. On the broad scan spectrum (Figure 3a), the major photoelectron peaks for niobium, calcium, oxygen, carbon, and an oxygen Auger peak are labeled. Before the sample was heated, the ratio of the integrated XPS peak intensities gives atomic ratios of Ca/Nb/O = 1.00:1.6:10.5 and C/Nb = 5.1:1 using the atomic sensitivity factors taken from Wagner et al.[53] and assuming a homogeneous distribution of elements within the total depth seen by XPS. The atomic concentrations of oxygen and carbon indicate that the sample contains a significant amount of organics (CH$_x$, C−O, and COOH).

After the sample was heated to a high temperature, the C concentration dropped markedly, as shown in Figure 3a, with the ratio of C/Nb decreasing by 7-fold to 0.71:1. The atomic ratio of Ca/Nb/O also changed to 1.00:1.5:4.7, which is very close to that expected based on the bulk chemical formula, Ca$_4$Nb$_6$O$_{19}$. The comparison of O 1s, Nb 3d, and Ca 2p core-level spectra before and after the heating procedure is also shown in Figure 3. Besides a small shift (∼0.2 eV) to a lower binding energy, there is no broadening or line shape change for the Nb 3d and Ca 2p peaks, which indicates no or negligible oxidation state change for the two elements. The change for O 1s, however, is significant. The O 1s spectrum measured before the sample was heated is much broader, with a shoulder peak
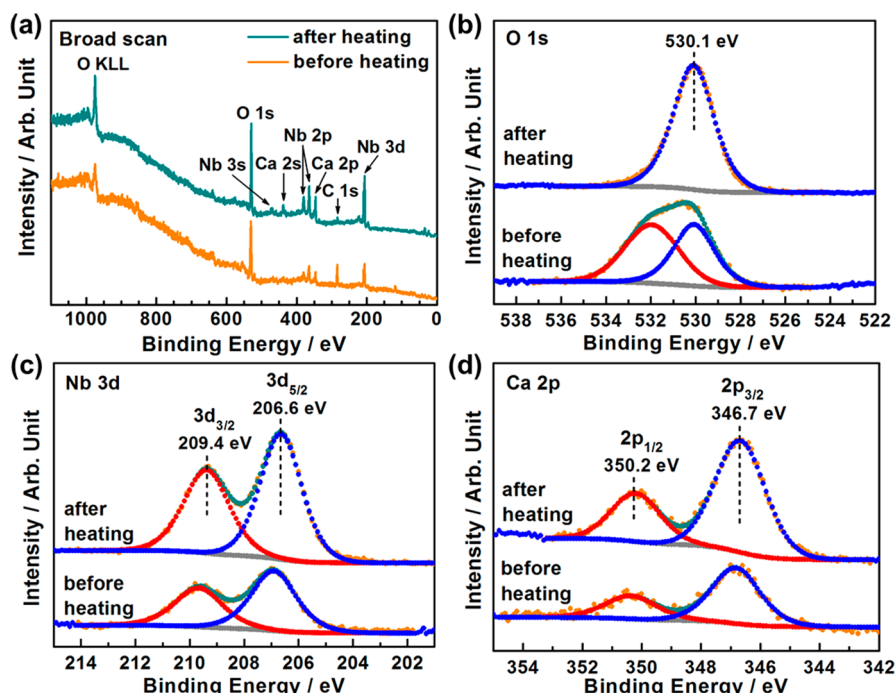
**Figure 3.** XPS spectra of 4 layers of $HCa_2Nb_3O_{10}(001)$ nanosheets deposited on $LiTaO_3$ heat detectors before and after heating to $\sim$725 K, which produces its dehydrated form: (a) broad scan, (b) O 1s, (c) Nb 3d, and (d) Ca 2p. The spectra measured before the sample being heated have been normalized so that the average broad scan intensity at 1050−1100 eV before heating matches that after heating.

above 532 eV BE, while the O 1s spectrum measured after the sample was heated shows a much more symmetric line shape. We attribute the change of the O 1s spectrum to the removal of adsorbed molecules containing O, which is also consistent with the decrease of relative atomic concentration of oxygen. (The O 1s BE range for the part that was removed is consistent with C−O and COOH functionalities.[53,58]) Previously, it has been shown that hydrocarbon impurities could be removed from perovskite-type $SrRuO_3$ films after annealing to >575 K in high oxygen pressure conditions.[59] For all the samples studied, there was always negligible intensity at the position of the N 1s peak in the broad scan XPS spectra both before and after heating.

### 3.3. Sticking Probability of Ag on dh-$HCa_2Nb_3O_{10}(001)$.
The amount of Ag atoms that chemically adsorb on the dh-$HCa_2Nb_3O_{10}(001)$ surface must be known to determine the true Ag coverage and to convert heats of adsorption measured by calorimetry into units of kJ/mol adsorbed. Figure 4 shows the sticking probability of Ag atoms on the dh-$HCa_2Nb_3O_{10}(001)$ surface at 300 K as a function of Ag coverage. One Ag monolayer (ML) is defined throughout as $1.38 \times 10^{15}$ atoms/cm$^2$, the number of Ag surface atoms per unit area on the Ag(111) surface. In the limit of zero coverage, the sticking probability of Ag on $HCa_2Nb_3O_{10}$ is 0.955 and increases rapidly to 0.98 at 1 ML coverage. The sticking probability increases slowly toward unit at higher coverages. This is expected because multilayer Ag films are known to have a near-unit sticking probability for Ag at 300 K.[14,15,57]

### 3.4. LEIS Study of the Ag Film Morphology on dh-$HCa_2Nb_3O_{10}(001)$.
The method used here to detect the morphology and growth mode of the Ag film (such as the average thickness and number density of growing nanoparticles) is based on measurements of the intensities of He$^+$ LEIS peaks associated with the substrate and the Ag metal itself, which essentially provides quantitative elemental analysis
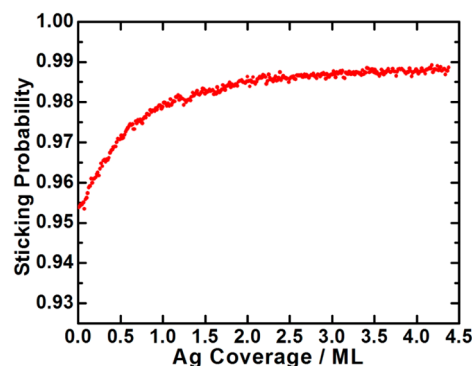


**Figure 4.** Sticking probability of Ag atoms on the dh-$HCa_2Nb_3O_{10}(001)$ surface (heated at $\sim$725 K for 10 min in an oxygen pressure of $2 \times 10^{-7}$ mbar) as a function of Ag coverage at 300 K. Each data point represents a pulse of $\sim$0.013 ML. One ML is defined as the atom density of Ag(111), which is 2.05 times the number of O atoms per area on the dh-$HCa_2Nb_3O_{10}(001)$ surface.

of the topmost atomic layer of the solid.[15,57,60,61] Here, we used He$^+$ LEIS at a primary energy of 1 keV.

Figure 5a shows the LEIS spectra for the starting dh-$HCa_2Nb_3O_{10}(001)$ surface (red dots) and for 1.1 ML adsorbed Ag (blue dots) at 300 K. For the starting dh-$HCa_2Nb_3O_{10}(001)$ surface, only an oxygen peak at $\sim$420 eV kinetic energy was detected above the baseline because the surface is O-terminated. (Hydrogen is too light to detect in LEIS.) After Ag was deposited on the surface, the intensity of the oxygen peak decreased and a silver peak at $\sim$860 eV kinetic energy appeared. We note that the absence of peaks for Ca and Nb (expected at 710 and 863 eV, respectively) in the spectrum of the starting surface helps confirm the quality of our crystals' surfaces. As shown in Figure 1, Nb is in the second atomic layer and Ca is in the third atomic layer of this structure. These
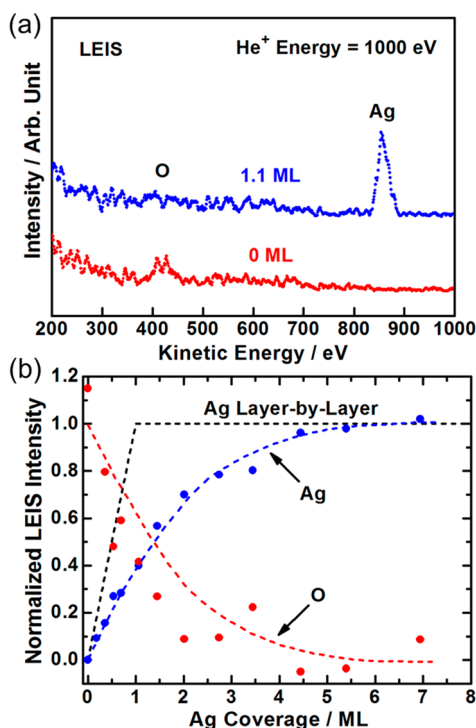
**Figure 5.** (a) He$^+$ LEIS spectra (at a primary energy of 1 keV) for the starting dh-HCa$_2$Nb$_3$O$_{10}$(001) surface (red dots) and for 1.1 ML adsorbed Ag (blue dots) at 300 K. (b) Integrated Ag (blue dots) and O (red dots) LEIS intensities as a function of Ag coverage at 300 K on the dh-HCa$_2$Nb$_3$O$_{10}$(001) surface (heated at ∼725 K for 10 min in an oxygen pressure of $2 \times 10^{-7}$ mbar). Ag and O peak intensities were normalized with respect to that from high Ag coverages and the starting dh-HCa$_2$Nb$_3$O$_{10}$(001) surface, respectively. The black dashed lines correspond to the normalized LEIS intensities that would be observed if Ag grew in a layer-by-layer fashion on a flat substrate. Note that the blue and red dashed curves are only to guide the reader's eye.

elements reside below the probe depth of He$^+$ LEIS at the primary beam energy of 1 keV used here (which is limited to the top-most surface layer of atoms, e.g., the atoms that are coordinatively unsaturated due to surface cleavage of the full 3D bulk structure). Peaks for Nb and Ca were reported in He$^+$ LEIS spectra for a similarly prepared Ca niobate monolayer,[62] but that study may not have used the very low total ion dose used here to prevent ion beam damage. That study used much higher ion energy (3 keV) as well. We note that the signal-to-noise ratio in Figure 5a is lower than in that study, which we attribute to our very low total ion dose and lower ion energy, as well as possibly a higher pass energy used in that earlier report.

Figure 5b shows the evolution of the integrated Ag and O LEIS intensities (normalized with respect to that from high Ag coverages and the starting dh-HCa$_2$Nb$_3$O$_{10}$(001) surface, respectively) as a function of Ag coverage on the dh-HCa$_2$Nb$_3$O$_{10}$(001) surface at 300 K. This provides a direct measurement of the fraction of the dh-HCa$_2$Nb$_3$O$_{10}$(001) surface covered by Ag particles (even if they are only one atom thick) because the He$^+$ ions are neutralized with essentially unit probability when they penetrate the electron density of a solid by an amount deeper than a small fraction of an atom and are thus not detected as a LEIS signal.[60] As seen in Figure 5b, the normalized LEIS intensities for both Ag and O change more slowly with Ag coverage than predicted by a layer-by-

layer growth model on a flat substrate (shown by the dashed black line for Ag). Note that the blue and red dashed lines in Figure 5b are not best fits to the Ag and O LEIS signals but are just used to guide the reader's eye.

We tried to fit these LEIS signals using the hemispherical cap model first introduced by Diebold et al.,[63] which assumes that all the nanoparticles have a hemispherical cap shape, the same diameter at any coverage (which increases with coverage), and the same number density at all coverages, but refined to consider shadowing effects.[61] This model cannot fit the data well. Specifically, it predicts that the LEIS signal for the metal would increase proportionally to the 2/3 power of the metal coverage up to ∼35% of the surface being covered,[61] whereas the Ag signal in Figure 5b increases linearly instead (as shown better in the expanded scale in Figure 6). The
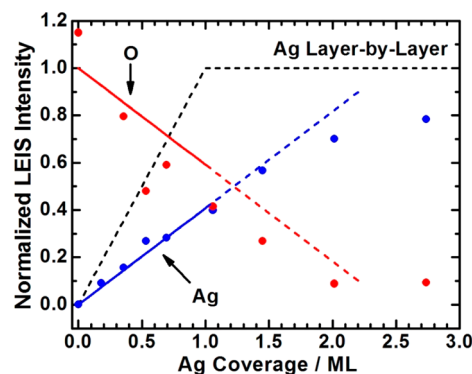


**Figure 6.** Integrated Ag (blue dots) and O (red dots) LEIS intensities versus Ag coverage up to 3 ML from Figure 5b. The blue solid line is a linear fit with a slope of 0.41 for the Ag LEIS signal up to 1 ML Ag coverage, above which the Ag LEIS signal starts to curve down so the blue dashed line after that is only a guide to the eye. The red line does not represent a best fit for the O LEIS signal but mirrors the blue line with respect to the normalized LEIS intensity at 50%. The black dashed lines correspond to the normalized LEIS intensities that would be observed if Ag grew in a layer-by-layer fashion on a flat substrate.

normalized Ag LEIS signal was fitted linearly with a slope of 0.41 in the first ML in Figure 6. The Ag layer-by-layer growth model in the first ML has a slope of 1. If Ag grew perfectly as flat 2-dimensional (2D) islands that are two atomic layers thick, with each layer having a packing density the same as our definition of 1 ML (i.e., the same as for bulk Ag(111)), one would expect a linear LEIS signal increase with a slope of 0.50, similar to what is observed. The straight-line fits in Figure 6 indicate that, on dh-HCa$_2$Nb$_3$O$_{10}$(001) at 300 K, Ag grows as flat 2D islands that are between 2 and 3 Ag layers thick until these cover ∼50% of the surface. Above 1.5 ML, the Ag LEIS signal starts to curve down and no longer follows the linear fit. This indicates that, above 1.5 ML, Ag mostly adds on top of existing Ag islands to form 3D particles, but also adds (more slowly) to their edges, eventually making a continuous 3D Ag film.

To further prove that the 2D islands are 2−3 Ag layers thick at low coverages, we calculated the average Ag particle thickness versus coverage from these Ag LEIS data (i.e., by dividing the Ag coverage in ML by the fraction of the surface covered by Ag particles from LEIS). The resulting island thickness as a function of Ag coverage at 300 K is shown in Figure 7. The inset shows a close-up of the low Ag coverage region. Below 1.5 ML coverage, the average Ag particle
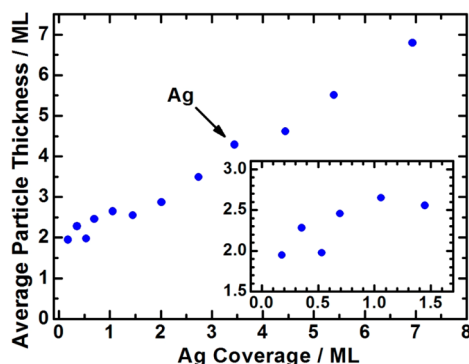
**Figure 7.** Average Ag nanoparticle thickness (as measured by LEIS) as a function of Ag coverage at 300 K. The inset shows a close-up of the low-coverage region. The thickness of 1 ML is 0.236 nm, which is the layer-to-layer separation between Ag(111) layers.

thickness increases slowly from 1.9 to 2.6 ML. Above 1.5 ML, the average Ag particle thickness increases faster, reaching 6.8 ML by 7 ML coverage when a continuous film first forms.

### 3.5. Heat of Adsorption of Ag Vapor on dh-HCa₂Nb₃O₁₀(001).

### 3.5. Heat of Adsorption of Ag Vapor on dh-$HCa_2Nb_3O_{10}$(001). Figure 8 shows the differential heat of
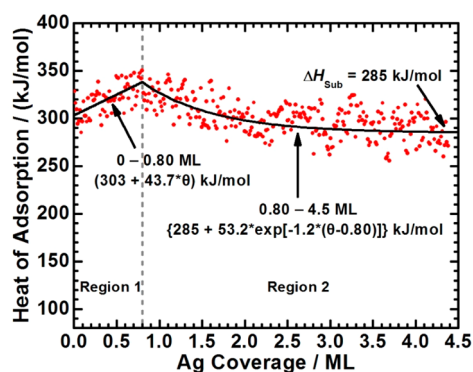


**Figure 8.** Differential heat of adsorption of Ag atoms on dh-$HCa_2Nb_3O_{10}$(001) surface (heated at ∼725 K for 10 min in an oxygen pressure of $2 \times 10^{-7}$ mbar) as a function of Ag coverage at 300 K. Ag coverage is separated by a gray dashed line into 2 regions, corresponding to different adsorption behaviors (see text). Note that the black lines are best fits to the data with a straight line in Region 1 and an exponential decay in Region 2.

adsorption of Ag on the dh-$HCa_2Nb_3O_{10}$(001) surface as a function of Ag coverage at 300 K, averaged over three experimental runs. We normalized the three runs individually by adjusting the absolute optical reflectivity of the starting surface (used in the heat signal calibration with heat from a He−Ne laser at 632 nm) to set the heat of adsorption at high coverages (>4 ML) equal to the known heat of sublimation of bulk Ag(s) (285 kJ/mol[64]). When individually normalized in this way, the three runs all showed the same coverage dependences of heats.

In Figure 8, Ag coverage was separated by a gray dashed line into two regions corresponding to different adsorption behaviors. In Region 1, the heat of adsorption is initially ∼303 kJ/mol and increases slowly to ∼338 kJ/mol by 0.8 ML. We attribute this initial rise to an increase in the average size (lateral dimension or effective diameter) of the Ag 2D islands (which were shown by LEIS earlier to have a nearly constant thickness of 2−3 atomic layers in this coverage range,

increasing slightly with coverage). This increase in size results in an increase in the average number of Ag−Ag nearest-neighbor bonds formed per added Ag atom.[14] Above 0.8 ML, the heat decreases exponentially toward the heat of sublimation of bulk Ag (285 kJ/mol[64]) by 4.5 ML (see Region 2). We attribute this slow drop to the simple kinetic competition between Ag atoms that adsorb in a structure similar to that seen at ∼0.6−0.8 ML (i.e., at the edges of large 2D islands of Ag that are 2−3 atoms thick with a heat near 338 kJ/mol) or in a structure more similar to adsorbing on top of a thick 3D film (i.e., on top of large 2D (and later, 3D) islands of Ag with a heat near 285 kJ/mol). As the coverage increases, the Ag atoms will naturally have a greater and greater probability to adsorb in the second type structure, so the heat decreases asymptotically to 285 kJ/mol. The integral (i.e., coverage-averaged) heat of adsorption in the first ML is 320 kJ/mol.

The heats of adsorption of Ag atoms have been measured on MgO(100) and on reducible oxide surfaces (e.g., $CeO_{2-x}$(111) and $Fe_3O_4$(111)) previously.[14,15,57] For comparison, the initial heats of Ag adsorption were 176, 200, 220, and 230 kJ/mol on MgO(100), $CeO_{1.9}$(111), $CeO_{1.8}$(111), and $Fe_3O_4$(111), respectively.[14,15,57] The much stronger binding strength of Ag atoms seen here on the dh-$HCa_2Nb_3O_{10}$(001) surface (303 kJ/mol) indicates that this mixed-oxide support stabilizes Ag nanoparticles better than those simple oxide supports. Strong interfacial interactions between late transition metal/metal oxide nanoparticles and the layered dh-$HCa_2Nb_3O_{10}$(001) nanosheets have also been found by liquid-phase isothermal titration calorimetry (ITC), electron microscopy, and density functional theory (DFT) calculations, showing that nanoparticles on supports with exothermic heats of interaction were stabilized against sintering.[37,38] Our high heats of adsorption at low coverages measured in UHV agree with these findings.

### 3.6. Chemical Reaction between Ag Atoms and dh-$HCa_2Nb_3O_{10}$(001).

Figure 9 shows the XPS spectra and peak fits of Ag 3d for the adsorbed Ag nanoparticles and O 1s, Nb 3d, and Ca 2p in the dh-$HCa_2Nb_3O_{10}$ support at 0 and 1.1 ML Ag coverages. Each peak was fitted with the product of a Gaussian and Lorentzian function after subtraction of a Shirley baseline.[65,66] The overlapping Ag 3d doublets (blue dots) and Nb 2p doublets (red dots) are deconvoluted in Figure 9a. No noticeable change in line shape was detected for Nb 3d and Ca 2p peaks after Ag deposition, but they all shifted to higher binding energies (BE) by 0.3−0.4 eV (see Figure 10 below). For O 1s, a second peak at ∼2 eV higher BE appeared after Ag was deposited on the surface. This Ag-induced component is labeled as $O^2$, and the original and main O 1s component at a lower BE is labeled as $O^1$.

Figure 10 shows the core−electron XPS BE shifts for Ag and for all the elements in the dh-$HCa_2Nb_3O_{10}$ support as a function of Ag coverage at 300 K. The BE shift of O 1s in Figure 10b is represented by the BE shift of the O 1s peak's centroid or "center line" (the integrated area is the same on both sides of the line). The BE of Ag $3d_{5/2}$ starts high after the first Ag dose (0.18 ML), drops rapidly by 0.35 eV after the second Ag dose (0.36 ML), and then stays nearly constant at higher coverages, eventually decreasing slightly to reach the BE of 367.9 eV expected for bulk Ag(s)[53] at 6.8 ML. The high Ag BE at the lowest coverage is attributed mainly to electron transfer from Ag to the dh-$HCa_2Nb_3O_{10}$ support at very low coverage, which causes the Ag to be partially positively charged (i.e., higher XPS BE than at higher coverages where Ag becomes bulklike). Janik and co-workers also discovered from
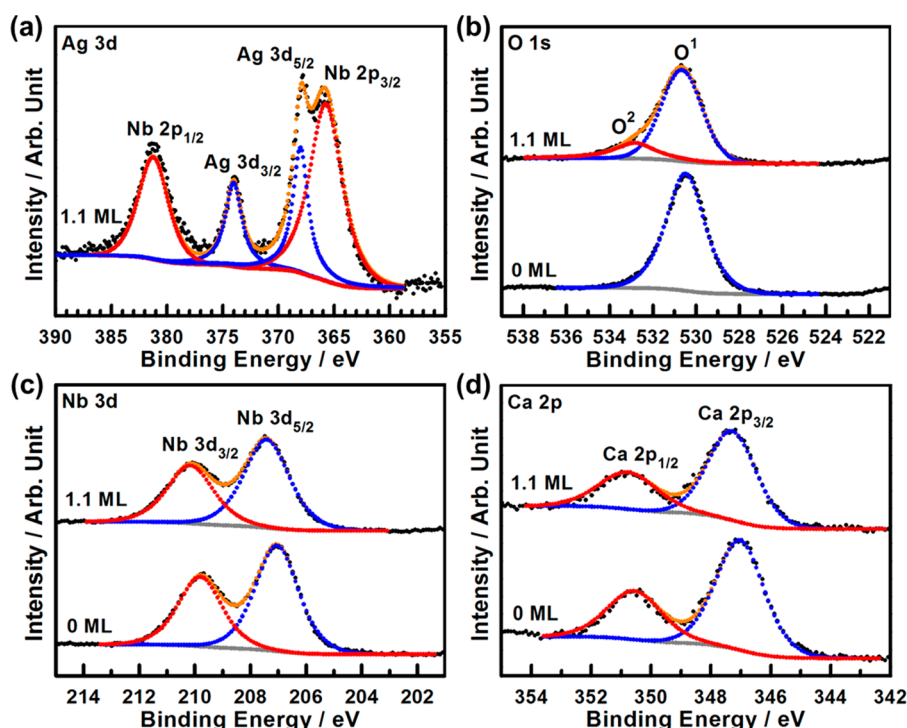
**Figure 9.** XPS spectra ($h\nu$ = 1486.6 eV) and peak fits of the elements: (a) Ag 3d for the adsorbed Ag nanoparticles and (b) O 1s, (c) Nb 3d, and (d) Ca 2p in the dh-HCa$_2$Nb$_3$O$_{10}$ support, plotted for the starting clean dh-HCa$_2$Nb$_3$O$_{10}$(001) surface and after adsorbing 1.1 ML of Ag at 300 K. The O 1s peak at 1.1 ML Ag coverage was fitted with two components labeled as O$^1$, ascribed to the nonbonding O atoms (mostly subsurface O atoms) of the perovskite support, and O$^2$, the surface oxygen atoms that are in closer contact to the cationically adsorbed Ag. The overlapping Ag 3d doublets (blue dots) and Nb 2p doublets (red dots) are deconvoluted in (a).
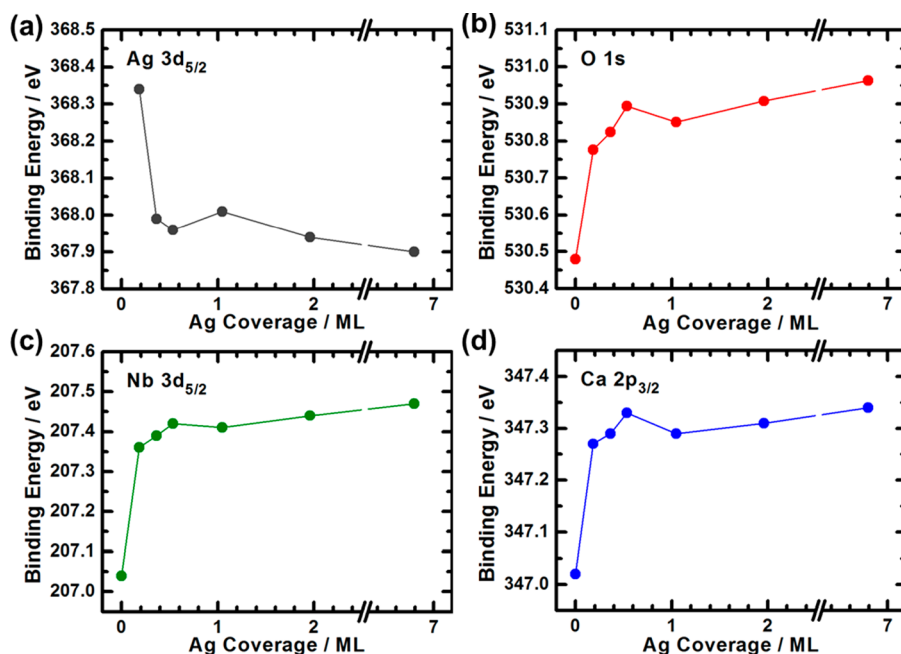


**Figure 10.** Core−electron XPS binding energy shifts with Ag coverage at 300 K for (a) Ag 3d$_{5/2}$ for the adsorbed Ag nanoparticles and (b) O 1s, (c) Nb 3d$_{5/2}$, and (d) Ca 2p$_{3/2}$ in the dh-HCa$_2$Nb$_3$O$_{10}$(001) support. The BE shift of the O 1s peak in (b) is represented by the BE shift of the O 1s peak's centroid or center line, on both sides of which the integrated area is the same. All spectra have been energy-referenced to the Ag 3d$_{5/2}$ peak for bulk Ag(s) (367.9 eV).[53]

DFT calculations and Bader charge analysis that, for all the adsorbed transition metals they studied, there was significant transfer of electron density from the metal atoms to the HCa$_2$Nb$_3$O$_{10}$(001) support, with the metal adatom having a charge of +0.68 in the case of Ag,[38] consistent with our

observation. As seen here, the Ag stops donating electrons to the oxide support at higher coverages, so the Ag BE stabilizes. The XPS BEs of metal nanoparticles (even when neutral) shift weakly to higher BE with decreasing particle size because there is less final-state relaxation of the core hole via screening by

conduction electrons in smaller particles than in bulk metal.[67−69] (The strength of the screening increases with metal coverage or particle size.) This effect may be responsible for the small Ag BE shifts at higher coverages here.

The core-level BEs for all the support elements (and the residual C impurity) shift by ∼0.3 eV to higher BE with the first Ag dose (Figure 10). As noted earlier, this Ag has a significant positive charge. These uniform shifts of the support elements' XPS peaks indicate that at least some of the electron density from this $Ag^{\delta+}$ transfers deeper into the sample than the XPS probe depth. This gives rise to a band-bending-like effect, where all the atoms within the XPS probe depth feel this positive charge (of $Ag^{\delta+}$ nearby), and so all their electrons get stabilized, shifting to higher BEs by the same ∼0.3 eV. This same effect has frequently been seen upon metal adsorption on thick semiconducting oxide crystals, where the electron donated from the metal is delocalized deep into the bulk of the oxide, so that the surface atoms of the oxide feel the nearby metal atom's positive charge and shift to higher BE upon metal adsorption.[68] After that first Ag dose, the new Ag is neutral and the effect stops, so the BEs of the support elements nearly stabilize (increasing only slightly by an additional ∼0.1 eV for Nb and Ca and by ∼0.2 eV for O). The $O^2$ component of the O 1s peak appeared after the first Ag dose (0.18 ML), and because it is ∼2 eV higher in BE than the main peak, it dominates the overall shift of the O 1s centroid.

Figure 11 shows the XPS intensity of the $O^2$ component of the O 1s peak normalized to the total O 1s intensity of the Ag-
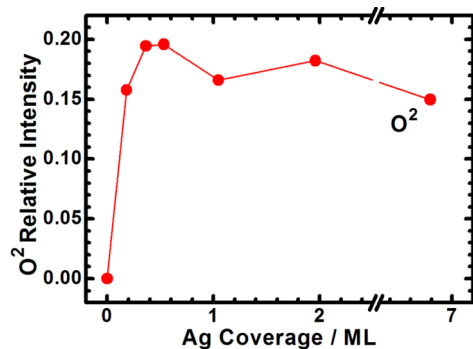


**Figure 11.** Integrated XPS intensity of the $O^2$ component of the O 1s peak, normalized to the total integrated O 1s peak for the starting surface (before dosing Ag).

free starting surface. As seen, the $O^2$ intensity almost plateaus already after the first dose of Ag (0.18 ML), just as the electron transfer from Ag to the support occurs mainly from the Ag in this first 0.18 ML, where the Ag takes the form of $Ag^{\delta+}$. This indicates that the $O^2$ atoms are those that are closest to this $Ag^{\delta+}$. This raises the question: How deeply are we measuring this $O^2$ component? The mean free path of the O 1s electrons at their kinetic energy measured here is estimated to be 1.67 nm based on eq 5 in ref 70. Because detection is normal to the surface, this equals the O 1s probe depth. There are ∼8 layers of O atoms within this depth of the dh-$HCa_2Nb_3O_{10}$(001) surface (see Figure 1). The large contribution from the $O^2$ component (∼16% after 0.18 ML) suggests that both of the first two layers of O atoms must be included in this component because the first O layer includes only ∼9% of the O atoms in this probe depth. The first two O layers hold 27% because there are twice as many O atoms in the second layer. The

observed 16% contribution from the $O^2$ component suggests that it corresponds to all the O atoms in the first O layer and roughly half of those in the second layer. At the Ag coverage of 0.18 ML, this corresponds to roughly five $O^2$-type O atoms created for every $Ag^{\delta+}$ atom. An idealized c(2 × 2)-Ag overlayer on dh-$HCa_2Nb_3O_{10}$(001) (which corresponds to a similar coverage of 0.24 ML) would have one $Ag^{\delta+}$ for every two surface O atoms. It appears that both of these surface oxygen atoms plus the two or three nearest O atoms in the second layer would need to have O 1s binding energies strongly affected by each $Ag^{\delta+}$ to explain the large XPS signal from this $O^2$ component. This does not seem unreasonable.

**3.7. Adhesion Energy and Sinter Resistance for Ag Adsorption on dh-$HCa_2Nb_3O_{10}$(001).** The connection between adsorption and adhesion energies has been discussed in detail elsewhere,[14,68] and their mathematical relationship is represented by[14]

$$\sum_n \Delta H_{ads} = -n \cdot \Delta H_{sub} + (1 + f_r) \cdot A \cdot \gamma_{\nu/m} - A \cdot E_{adh} \quad (1)$$

where $\sum_n \Delta H_{ads}$ is the sum of the adsorption enthalpies over $n$ metal adatoms, $\Delta H_{sub}$ is the metal's bulk sublimation enthalpy, $A$ is the area covered by the metal particles, $f_r$ is the roughness factor to account for the surface roughness of the metal particles, $\gamma_{\nu/m}$ is the surface energy of the bulk metal solid ($\gamma_{\nu/m}$ is 1.22 $J/m^2$ for bulk Ag[5,13−15]), and $E_{adh}$ is the metal's adhesion energy to the support. Our LEIS results show that Ag grows as 2D islands that cover most of the surface before thickening and that ∼96% of the surface is covered by Ag already by 4.4 ML. This indicates that the surface is very smooth at 4.5 ML, so we will assume that $f_r$ is 1.00 here.

To estimate the adhesion energy for Ag adsorption on dh-$HCa_2Nb_3O_{10}$(001) using eq 1, we must integrate the heat of adsorption versus coverage up to a coverage where $\Delta H_{ads}$ is no longer different from $\Delta H_{sub}$.[47] Using the data from Figure 8 and integrating up to 4.5 ML, the adhesion energy for Ag adsorption on dh-$HCa_2Nb_3O_{10}$(001) is estimated to be 4.33 $J/m^2$. This is larger than twice the surface energy of Ag (2 × 1.22 $J/m^2$), which means that Ag wets this surface at equilibrium.[68]

For comparison, Ag growth on MgO(100), $CeO_{1.9}$(111), and $Fe_3O_4$(111) at 300 K gives number densities of 2.5 × 10^{12}, 4.0 × 10^{12}, and 4.0 × 10^{12} particles/$cm^2$ and adhesion energies of 0.3 ± 0.3, 2.3 ± 0.3, and 2.5 ± 0.3 $J/m^2$, respectively.[13−15,57] The higher adhesion energy of Ag to dh-$HCa_2Nb_3O_{10}$(001) indicates a very strong interaction between Ag(s) and the dh-$HCa_2Nb_3O_{10}$(001) surface.

This large adhesion energy of Ag to this Ca niobate(001) surface helps explain the stabilization of Rh nanoparticles against sintering reported on this same Ca niobate support.[37] While Ag and Rh are different, we have found that the adhesion energies of late transition metals to a given oxide support surface strongly correlate with each other and that when one such metal element has a higher adhesion energy to one given oxide surface compared to another so too do all the late transition metals.[12] As we have also shown, the higher the $E_{adh}$, the lower is the metal atom's chemical potential at a given particle size and the slower is the sintering rate.[12] This is qualitatively consistent with the earlier explanation for this unusually strong sinter-resistance imparted by this Ca niobate support based on solution-phase adsorption calorimetry and DFT calculations.[37,38] We can use the adhesion energy correlation mentioned earlier together with the value measured here for Ag on this Ca niobate(001) surface (4.33 $J/m^2$) to

predict $E_{adh}$ for other late transition metals to this mixed oxide surface. That correlation showed that $E_{adh}$ increases linearly with $[(\Delta H_{sub,M} - \Delta H_{f,MOx})/N_A]/\Omega_M^{2/3}$, which is a measure of the oxophilicity of the metal element per unit surface area.[12] Here, $\Delta H_{sub,M}$ is the bulk heat of sublimation of the metal M, $\Delta H_{f,MOx}$ is the heat of formation of its most stable bulk oxide (per mole of metal atoms), and $\Omega_M$ is the volume per atom in the bulk metal, so that $\Omega_M^{2/3}$ provides an estimate of the area per metal atom at the interface. The slope is 0.146 for the two oxides that have been studied, and this $x$-axis value (oxophilicity per area) for Ag is 7.5 J/m$^2$.[12] For Rh, this $x$ value is 23 J/m$^2$. Assuming the same slope as found for the other oxides, this correlation can be extrapolated from this $E_{adh}$ value for Ag (4.33 J/m$^2$) to predict that $E_{adh}$ equals ~6.6 J/m$^2$ for Rh to this Ca niobate(001) surface. This is larger than twice the surface energy of Rh ($2 \times 2.33$ J/m$^2$), which means that Rh is also predicted to wet this surface at equilibrium. (The surface energy of Rh used here is from ref 71.)

The question arises as to why the adhesion energy of Ag (and probably other later transition metals) is higher to this Ca niobate surface than to other oxide surfaces that have been studied (MgO(100), CeO$_{1.9}$(111), and Fe$_3$O$_4$(111)). We have shown that the adhesion energies of the same late transition metal to different oxide surfaces (divided by the number of moles of coordinatively unsaturated surface oxygen atoms per unit area) decrease crudely with the enthalpy cost (per mole of O atoms) to reduce that oxide to the pure metal or, if that metal has a stable oxide of lower oxidation state, to that next lower oxide plus O$_2$(gas), calculated using standard heats of formation.[12,72] There are ~$6.74 \times 10^{14}$ O atoms/cm$^2$ on this Ca niobate surface, which is less than on these other three oxide surfaces, so that density does not explain the high adhesion energy here. We do not know of thermodynamic data that would allow us to estimate the enthalpy cost to reduce this Ca niobate to its next lower oxidation state, but it is relatively easy to partially reduce it.[73] It has also been proposed on the basis of DFT calculations that the strength of bonding of single late transition metal atoms to different oxide surfaces correlates inversely with the oxygen vacancy formation energy of the oxide.[74] Although these results are promising, it seems that we are not yet able to predict how the adhesion energy for a given metal varies between different oxide surfaces. Quantum mechanical calculations may help achieve this in the future. For example, DFT calculations have shown that single transition metal atoms and 4-atom metal clusters bond more strongly to Ca niobate than to silica surfaces, consistent with isothermal titration calorimetry measurements.[38]

In single-crystal adsorption calorimetry, our group has often seen evidence for the presence of more strongly bonding defect sites such as terrace-edge or step sites as a higher heat of adsorption during the first few pulses of gas, after which the heat drops as the defect sites get saturated.[75−77] For example, this was clearly seen for Cu and Ni adsorption on CeO$_2$(111) at 300 K, where these defects (which cover only ~5% of the surface) had higher heats by 30−60 kJ/mol than terraces.[76,77] However, this was not seen for Ag or Au on CeO$_2$(111) at 300 K, even when prepared in the same way.[57,78] Nevertheless, comparing heats at 100 versus 300 K did show that Au also binds more strongly initially at 300 K, where it can more easily diffuse to defects at terrace edges than at 100 K.[78] Those data were interpreted in terms of a 27 kJ/mol higher heart of adsorption at these defects. Thus, it seems likely that Ag also binds more strongly to defects at terrace edges on CeO$_2$(111)

than to terrace sites. The same is likely to also be the case here on this Ca niobate surface, and perhaps that could be seen by doing experiments also at 100 K (which was not possible in the apparatus used here). Still, there is nothing in the data measured here to suggest that there was a larger contribution from defect sites than seen in our studies of metal adsorption on other single crystal oxide surfaces. Indeed, this is expected given the large size of the nanosheet crystals used here to prepare this surface. It is important to note that the height of the nanosheet edges (ca. 1.5 nm) is very small relative to the lateral dimensions of the single-crystalline Ca niobate nanosheets, which are typically in the range of hundreds of nm. Therefore, we do not expect that reaction at edge sites contributed significantly to the measured thermochemical values here.

## 4. CONCLUSIONS

Unilamellar HCa$_2$Nb$_3$O$_{10}$ nanosheets were easily deposited onto a LiTaO$_3$ heat detector as single-crystalline thin films using LB techniques. The AFM images show that these nanosheets are flat and have an average lateral dimension larger than 1 $\mu$m (the ratio of terrace to sheet-edge sites is huge). To obtain a relatively clean, dehydrated HCa$_2$Nb$_3$O$_{10}$(001) surface, the nanosheets were first heated to 725 K in a low oxygen pressure. These results demonstrate for the first time a new and easy way to apply surface science techniques derived for simple single-crystal surfaces to the complex surfaces of mixed oxides, using LB-deposited perovskite nanosheets. The He$^+$ LEIS and adsorption calorimetry results show that Ag grows on the dh-HCa$_2$Nb$_3$O$_{10}$(001) surface as 2D islands that are mostly two layers and some three layers thick with a coverage-averaged heat of adsorption of ~320 kJ/mol in the first monolayer. As the Ag coverage increases, Ag atoms add on top of the 2D islands, making 3D nanoparticles and eventually a continuous 3D film, with the heat of adsorption reaching the sublimation enthalpy of bulk Ag(s), 285 kJ/mol. A very high adhesion energy of Ag(s) to dh-HCa$_2$Nb$_3$O$_{10}$(001) of 4.33 J/m$^2$ is estimated from the heats of adsorption and explains why this dh-HCa$_2$Nb$_3$O$_{10}$ support imparts unusual stability against sintering to transition metal nanoparticles. At very low coverages, Ag is in the form of Ag$^{\delta+}$, which causes a ~2 eV shift to higher binding energy of the O 1s XPS peaks of nearby O atoms in the first two layers of the dh-HCa$_2$Nb$_3$O$_{10}$(001) support. Some of the electron density from this Ag$^{\delta+}$ transfers deeper into the sample than the XPS probe depth, causing the ~0.3 eV band-bending seen in all the support elements' core levels. Above 0.18 ML, Ag adsorbs in neutral form.

## ■ AUTHOR INFORMATION

### Corresponding Author

**Charles T. Campbell** − *Department of Chemistry, University of Washington, Seattle, Washington 98195-1700, United States;* ⓘ orcid.org/0000-0002-5024-8210; Email: charliec@uw.edu

### Authors

**Wei Zhang** − *Department of Chemistry, University of Washington, Seattle, Washington 98195-1700, United States*

**Ritesh Uppuluri** − *Department of Chemistry, The Pennsylvania State University, University Park, Pennsylvania 16802, United States*

**Thomas E. Mallouk** − *Department of Chemistry, The Pennsylvania State University, University Park, Pennsylvania 16802, United States; Department of Chemistry, University of*

*Pennsylvania, Philadelphia, Pennsylvania 19104, United States;*
*International Centre for Materials Nanoarchitectonics (WPI-MANA), National Institute for Materials Science (NIMS),*
*Tsukuba, Ibaraki 305-0044, Japan;* ⓘ orcid.org/0000-0003-4599-4208

Complete contact information is available at:
https://pubs.acs.org/10.1021/jacs.0c05044

**Notes**
The authors declare no competing financial interest.

## REFERENCES

(1) Haruta, M. Size-and support-dependency in the catalysis of gold. *Catal. Today* **1997**, *36*, 153−166.

(2) Mostafa, S.; Behafarid, F.; Croy, J. R.; Ono, L. K.; Li, L.; Yang, J. C.; Frenkel, A. I.; Cuenya, B. R. Shape-dependent catalytic properties of Pt nanoparticles. *J. Am. Chem. Soc.* **2010**, *132*, 15714−15719.

(3) Valden, M.; Lai, X.; Goodman, D. W. Onset of Catalytic Activity of Gold Clusters on Titania with the Appearance of Nonmetallic Properties. *Science* **1998**, *281*, 1647−1650.

(4) Goodman, D. W. Model Studies in Catalysis Using Surface Science Probes. *Chem. Rev.* **1995**, *95*, 523−536.

(5) Campbell, C. T. The Energetics of Supported Metal Nanoparticles: Relationships to Sintering Rates and Catalytic Activity. *Acc. Chem. Res.* **2013**, *46*, 1712−1719.

(6) Deshpande, P. A.; Hegde, M. S.; Madras, G. Pd and Pt ions as highly active sites for the water−gas shift reaction over combustion synthesized zirconia and zirconia-modified ceria. *Appl. Catal., B* **2010**, *96*, 83−93.

(7) He, Q.; Mukerjee, S.; Zeis, R.; Parres-Esclapez, S.; Illán-Gómez, M. J.; Bueno-López, A. Enhanced Pt stability in $MO_2$ (M=Ce, Zr or $Ce_{0.9}Zr_{0.1}$)-promoted Pt/C electrocatalysts for oxygen reduction reaction in PAFCs. *Appl. Catal., A* **2010**, *381*, 54−65.

(8) Kambolis, A.; Matralis, H.; Trovarelli, A.; Papadopoulou, C. Ni/$CeO_2$-$ZrO_2$ catalysts for the dry reforming of methane. *Appl. Catal., A* **2010**, *377*, 16−26.

(9) Zhao, M.; Wang, H.; Cai, L.; Zhu, Y.; Gong, M.; Chen, Y. Effect of Different Supports on Performance of Palladium Methanol Decomposition Catalyst. *Rare Metal Mater. Eng.* **2010**, *39*, 519−522.

(10) Zhu, H.; Razzaq, R.; Li, C.; Muhmmad, Y.; Zhang, S. Catalytic Methanation of Carbon Dioxide by Active Oxygen Material $Ce_xZr_{1−x}O_2$ Supported Ni−Co Bimetallic Nanocatalysts. *AIChE J.* **2013**, *59*, 2567−2576.

(11) Campbell, C. T.; Sellers, J. R. V. Enthalpies and Entropies of Adsorption on Well-Defined Oxide Surfaces: Experimental Measurements. *Chem. Rev.* **2013**, *113*, 4106−4135.

(12) Campbell, C. T.; Mao, Z. Chemical Potential of Metal Atoms in Supported Nanoparticles: Dependence upon Particle Size and Support. *ACS Catal.* **2017**, *7*, 8460−8466.

(13) Farmer, J. A.; Campbell, C. T. Ceria Maintains Smaller Metal Catalyst Particles by Strong Metal-Support Bonding. *Science* **2010**, *329*, 933−936.

(14) Larsen, J. H.; Ranney, J. T.; Starr, D. E.; Musgrove, J. E.; Campbell, C. T. Adsorption energetics of Ag on MgO(100). *Phys. Rev. B: Condens. Matter Mater. Phys.* **2001**, *63*, 195410.

(15) Sharp, J. C.; Yao, Y. X.; Campbell, C. T. Silver Nanoparticles on $Fe_3O_4$(111): Energetics by Ag Adsorption Calorimetry and Structure by Surface Spectroscopies. *J. Phys. Chem. C* **2013**, *117*, 24932−24936.

(16) Compton, O. C.; Carroll, E. C.; Kim, J. Y.; Larsen, D. S.; Osterloh, F. E. Calcium niobate semiconductor nanosheets as catalysts for photochemical hydrogen evolution from water. *J. Phys. Chem. C* **2007**, *111*, 14589−14592.

(17) Li, B.-W.; Osada, M.; Ozawa, T. C.; Ebina, Y.; Akatsuka, K.; Ma, R.; Funakubo, H.; Sasaki, T. Engineered interfaces of artificial perovskite oxide superlattices via nanosheet deposition process. *ACS Nano* **2010**, *4*, 6673−6680.

(18) Schaak, R. E.; Mallouk, T. E. Self-assembly of tiled perovskite monolayer and multilayer thin films. *Chem. Mater.* **2000**, *12*, 2513−2516.

(19) Song, Y.; Iyi, N.; Hoshide, T.; Ozawa, T. C.; Ebina, Y.; Ma, R.; Miyamoto, N.; Sasaki, T. Accordion-like swelling of layered perovskite crystals via massive permeation of aqueous solutions into 2D oxide galleries. *Chem. Commun.* **2015**, *51*, 17068−17071.

(20) Treacy, M. M. J.; Rice, S. B.; Jacobson, A. J.; Lewandowski, J. T. Electron microscopy study of delamination in dispersions of the perovskite-related layered phases $K[Ca_2Na_{n−3}Nb_nO_{3n−1}]$: evidence for single-layer formation. *Chem. Mater.* **1990**, *2*, 279−286.

(21) Akatsuka, K.; Haga, M.-a.; Ebina, Y.; Osada, M.; Fukuda, K.; Sasaki, T. Construction of Highly Ordered Lamellar Nanostructures through Langmuir−Blodgett Deposition of Molecularly Thin Titania Nanosheets Tens of Micrometers Wide and Their Excellent Dielectric Properties. *ACS Nano* **2009**, *3*, 1097−1106.

(22) Keller, S. W.; Kim, H.-N.; Mallouk, T. E. Layer-by-Layer Assembly of Intercalation Compounds and Heterostructures on Surfaces: Toward Molecular ″Beaker″ Epitaxy. *J. Am. Chem. Soc.* **1994**, *116*, 8817−8818.

(23) Ma, R.; Sasaki, T. Two-Dimensional Oxide and Hydroxide Nanosheets: Controllable High-Quality Exfoliation, Molecular Assembly, and Exploration of Functionality. *Acc. Chem. Res.* **2015**, *48*, 136−143.

(24) Muramatsu, M.; Akatsuka, K.; Ebina, Y.; Wang, K.; Sasaki, T.; Ishida, T.; Miyake, K.; Haga, M. -a. Fabrication of Densely Packed Titania Nanosheet Films on Solid Surface by Use of Langmuir−Blodgett Deposition Method without Amphiphilic Additives. *Langmuir* **2005**, *21*, 6590−6595.

(25) Diaz, S.; Zhu, J.; Harris, J.; Goetsch, P.; Merte, L.; Campbell, C. T. Heats of adsorption of Pb on pristine and electron-irradiated poly(methyl methacrylate) by microcalorimetry. *Surf. Sci.* **2005**, *598*, 22−34.

(26) Lownsbury, J. M.; Santos-Lopez, I. A.; Zhang, W.; Campbell, C. T.; Yu, H. Y. S.; Liu, W. G.; Cramer, C. J.; Truhlar, D. G.; Wang, T.; Hupp, J. T.; Farha, O. K. Calcium Vapor Adsorption on the Metal-Organic Framework NU-1000: Structure and Energetics. *J. Phys. Chem. C* **2016**, *120*, 16850−16862.

(27) Royer, S.; Duprez, D.; Can, F.; Courtois, X.; Batiot-Dupeyrat, C.; Laassiri, S.; Alamdari, H. Perovskites as Substitutes of Noble Metals for Heterogeneous Catalysis: Dream or Reality. *Chem. Rev.* **2014**, *114*, 10292−10368.

(28) Fang, M.; Kim, C. H.; Mallouk, T. E. Dielectric properties of the lamellar niobates and titanoniobates $AM_2Nb_3O_{10}$ and $ATiNbO_5$ (A = H, K, M = Ca, Pb), and their condensation products $Ca_4Nb_6O_{19}$ and $Ti_2Nb_2O_9$. *Chem. Mater.* **1999**, *11*, 1519−1525.

(29) Chen, Y.; Zhao, X.; Ma, H.; Ma, S.; Huang, G.; Makita, Y.; Bai, X.; Yang, X. Structure and dehydration of layered perovskite niobate with bilayer hydrates prepared by exfoliation/self-assembly process. *J. Solid State Chem.* **2008**, *181*, 1684−1694.

(30) Gao, H.; Shori, S.; Chen, X.; zur Loye, H.-C.; Ploehn, H. J. Quantitative analysis of exfoliation and aspect ratio of calcium niobate platelets. *J. Colloid Interface Sci.* **2013**, *392*, 226−236.

(31) Jacobson, A. J.; Lewandowski, J. T.; Johnson, J. W. Ion exchange of the layered perovskite $KCa_2Nb_3O_{10}$ by protons. *J. Less-Common Met.* **1986**, *116*, 137−146.

(32) Ebina, Y.; Sasaki, T.; Harada, M.; Watanabe, M. Restacked perovskite nanosheets and their Pt-loaded materials as photocatalysts. *Chem. Mater.* **2002**, *14*, 4390−4395.

(33) Liang, S. J.; Zhu, S. Y.; Chen, Y.; Wu, W. M.; Wang, X. C.; Wu, L. Rapid template-free synthesis and photocatalytic performance of

visible light-activated SnNb$_2$O$_6$ nanosheets. *J. Mater. Chem.* **2012**, *22*, 2670−2678.

(34) Ma, X. D.; Jiang, D. L.; Xiao, P.; Jin, Y.; Meng, S. C.; Chen, M. 2D/2D heterojunctions of WO$_3$ nanosheet/K$^+$Ca$_2$Nb$_3$O$_{10}^-$ ultrathin nanosheet with improved charge separation efficiency for significantly boosting photocatalysis. *Catal. Sci. Technol.* **2017**, *7*, 3481−3491.

(35) Park, S.; Song, H. J.; Lee, C. W.; Hwang, S. W.; Cho, I. S. Enhanced Photocatalytic Activity of Ultrathin Ba$_5$Nb$_4$O$_{15}$ Two-Dimensional Nanosheets. *ACS Appl. Mater. Interfaces* **2015**, *7*, 21860−21867.

(36) Wang, Y.; Ren, Y.; Luo, J. J.; Hao, Q. Y.; Li, B.; Gao, Z.; Hu, Y. W.; Lin, D.; Tang, K. B. Preparation of ultrathin perovskite nanosheets by the exfoliation of H$_2$CaTa$_2$O$_7$ for high-performance lead removal from water. *RSC Adv.* **2016**, *6*, 113671−113680.

(37) Strayer, M. E.; Binz, J. M.; Tanase, M.; Kamali Shahri, S. M.; Sharma, R.; Rioux, R. M.; Mallouk, T. E. Interfacial bonding stabilizes rhodium and rhodium oxide nanoparticles on layered Nb oxide and Ta oxide supports. *J. Am. Chem. Soc.* **2014**, *136*, 5687−5696.

(38) Strayer, M. E.; Senftle, T. P.; Winterstein, J. P.; Vargas-Barbosa, N. M.; Sharma, R.; Rioux, R. M.; Janik, M. J.; Mallouk, T. E. Charge transfer stabilization of late transition metal oxide nanoparticles on a layered niobate support. *J. Am. Chem. Soc.* **2015**, *137*, 16216−16224.

(39) Oshima, T.; Lu, D.; Ishitani, O.; Maeda, K. Intercalation of highly dispersed metal nanoclusters into a layered metal oxide for photocatalytic overall water splitting. *Angew. Chem., Int. Ed.* **2015**, *54*, 2698−2702.

(40) Li, B.-W.; Osada, M.; Ebina, Y.; Akatsuka, K.; Fukuda, K.; Sasaki, T. High thermal robustness of molecularly thin perovskite nanosheets and implications for superior dielectric properties. *ACS Nano* **2014**, *8*, 5449−5461.

(41) Chen, C.-J.; Harris, J. W.; Bhan, A. Kinetics of Ethylene Epoxidation on a Promoted Ag/$\alpha$-Al$_2$O$_3$ Catalyst—The Effects of Product and Chloride Co-Feeds on Rates and Selectivity. *Chem. - Eur. J.* **2018**, *24*, 12405−12415.

(42) Imamura, S.; Yamada, H.; Utani, K. Combustion activity of Ag/CeO$_2$ composite catalyst. *Appl. Catal., A* **2000**, *192*, 221−226.

(43) Kundakovic, L.; Flytzani-Stephanopoulos, M. Cu-and Ag-modified cerium oxide catalysts for methane oxidation. *J. Catal.* **1998**, *179*, 203−221.

(44) Zhang, D.-H.; Li, H.-B.; Li, G.-D.; Chen, J.-S. Magnetically recyclable Ag-ferrite catalysts: general synthesis and support effects in the epoxidation of styrene. *Dalton Trans.* **2009**, 10527−10533.

(45) Subramanian, V.; Roeder, R. K.; Wolf, E. E. Synthesis and UV−Visible-Light Photoactivity of Noble-Metal−SrTiO$_3$ Composites. *Ind. Eng. Chem. Res.* **2006**, *45*, 2187−2193.

(46) Zhang, W.; Campbell, C. T. Calorimetric Metal Vapor Adsorption Energies for Characterizing Industrial Catalyst Support Materials. *J. Catal.* **2020**, submitted.

(47) Stuckless, J.; Frei, N. A.; Campbell, C. T. A novel single-crystal adsorption calorimeter and additions for determining metal adsorption and adhesion energies. *Rev. Sci. Instrum.* **1998**, *69*, 2427−2438.

(48) Silva, M.; Costa, C. M.; Sencadas, V.; Paleo, A.; Lanceros-Méndez, S. Degradation of the dielectric and piezoelectric response of $\beta$-poly(vinylidene fluoride) after temperature annealing. *J. Polym. Res.* **2011**, *18*, 1451−1457.

(49) Kovář, M.; Dvořák, L.; Černý, S. Application of pyroelectric properties of LiTaO$_3$ single crystal to microcalorimetric measurement of the heat of adsorption. *Appl. Surf. Sci.* **1994**, *74*, 51−59.

(50) Hara, M.; Lean, J. T.; Mallouk, T. E. Photocatalytic Oxidation of Water by Silica-Supported Tris(4,4′-dialkyl-2,2′-bipyridyl)-ruthenium Polymeric Sensitizers and Colloidal Iridium Oxide. *Chem. Mater.* **2001**, *13*, 4668−4675.

(51) Maeda, K.; Mallouk, T. E. Comparison of two- and three-layer restacked Dion−Jacobson phase niobate nanosheets as catalysts for photochemical hydrogen evolution. *J. Mater. Chem.* **2009**, *19*, 4813−4818.

(52) King, D. A.; Wells, M. G. Molecular beam investigation of adsorption kinetics on bulk metal targets: Nitrogen on tungsten. *Surf. Sci.* **1972**, *29*, 454−482.

(53) Wagner, C. D.; Riggs, W. M.; Davis, L. E.; Moulder, J. F.; Muilenberg, G. E. *Handbook of X-ray Photoelectron Spectroscopy*; Perkin-Elmer Corp., Physical Electronics Division: Eden Prairie, MN, 1979.

(54) Okamoto, Y.; Ida, S.; Hyodo, J.; Hagiwara, H.; Ishihara, T. Synthesis and Photocatalytic Activity of Rhodium-Doped Calcium Niobate Nanosheets for Hydrogen Production from a Water/Methanol System without Cocatalyst Loading. *J. Am. Chem. Soc.* **2011**, *133*, 18034−18037.

(55) Giordano, L.; Baistrocchi, M.; Pacchioni, G. Bonding of Pd, Ag, and Au atoms on MgO(100) surfaces and MgO/Mo(100) ultra-thin films: A comparative DFT study. *Phys. Rev. B: Condens. Matter Mater. Phys.* **2005**, *72*, 115403.

(56) Freund, H.-J. Metal-supported ultrathin oxide film systems as designable catalysts and catalyst supports. *Surf. Sci.* **2007**, *601*, 1438−1442.

(57) Farmer, J. A.; Baricuatro, J. H.; Campbell, C. T. Ag Adsorption on Reduced CeO$_2$(111) Thin Films. *J. Phys. Chem. C* **2010**, *114*, 17166−17172.

(58) Beamson, G.; Briggs, D. *High Resolution XPS of Organic Polymers: The Scienta ESCA300 Database*; Wiley: New York, 1992.

(59) Shin, J.; Kalinin, S. V.; Lee, H. N.; Christen, H. M.; Moore, R. G.; Plummer, E. W.; Baddorf, A. P. Surface stability of epitaxial SrRuO$_3$ films. *Surf. Sci.* **2005**, *581*, 118−132.

(60) Brongersma, H. H.; Draxler, M.; de Ridder, M.; Bauer, P. Surface composition analysis by low-energy ion scattering. *Surf. Sci. Rep.* **2007**, *62*, 63−109.

(61) Campbell, C. T.; James, T. E. Ion scattering spectroscopy intensities for supported nanoparticles: The hemispherical cap model. *Surf. Sci.* **2015**, *641*, 166−169.

(62) Ida, S.; Takashiba, A.; Koga, S.; Hagiwara, H.; Ishihara, T. Potential Gradient and Photocatalytic Activity of an Ultrathin p−n Junction Surface Prepared with Two-Dimensional Semiconducting Nanocrystals. *J. Am. Chem. Soc.* **2014**, *136*, 1872−1878.

(63) Diebold, U.; Pan, J. M.; Madey, T. E. Growth mode of ultrathin copper overlayers on TiO$_2$(110). *Phys. Rev. B: Condens. Matter Mater. Phys.* **1993**, *47*, 3868−3876.

(64) Haynes, W. M. *CRC Handbook of Chemistry and Physics*, 96th ed.; CRC Press: 2015.

(65) Shirley, D. A. High-Resolution X-Ray Photoemission Spectrum of the Valence Bands of Gold. *Phys. Rev. B* **1972**, *5*, 4709−4714.

(66) Ansell, R. O.; Dickinson, T.; Povey, A. F.; Sherwood, P. M. A. X-ray photoelectron spectroscopic studies of electrode surfaces using a new controlled transfer technique: Part II. Results for a molybdenum electrode and the curve fitting procedure. *J. Electroanal. Chem. Interfacial Electrochem.* **1979**, *98*, 79−89.

(67) Wertheim, G. K.; DiCenzo, S. B.; Buchanan, D. N. E. Noble- and transition-metal clusters: The d bands of silver and palladium. *Phys. Rev. B: Condens. Matter Mater. Phys.* **1986**, *33*, 5384−5390.

(68) Campbell, C. T. Ultrathin metal films and particles on oxide surfaces: structural, electronic and chemisorptive properties. *Surf. Sci. Rep.* **1997**, *27*, 1−111.

(69) Wertheim, G. K.; DiCenzo, S. B. Cluster growth and core-electron binding energies in supported metal clusters. *Phys. Rev. B: Condens. Matter Mater. Phys.* **1988**, *37*, 844−847.

(70) Seah, M. P.; Dench, W. A. Quantitative electron spectroscopy of surfaces: A standard data base for electron inelastic mean free paths in solids. *Surf. Interface Anal.* **1979**, *1*, 2−11.

(71) Tyson, W. R.; Miller, W. A. Surface free energies of solid metals: Estimation from liquid surface tension measurements. *Surf. Sci.* **1977**, *62*, 267−276.

(72) Campbell, C. T.; Mao, Z. Correction to "Chemical Potential of Metal Atoms in Supported Nanoparticles: Dependence upon Particle Size and Support. *ACS Catal.* **2018**, *8*, 8763−8764.

(73) Draskovic, T. I.; Wang, T.; Henderson, C. N.; Mallouk, T. E. Protonic and electronic conductivity of the layered perovskite oxides

$HCa_2Nb_3O_{10}$ and $Ca_4Nb_6O_{19}$. *Int. J. Hydrogen Energy* **2014**, *39*, 4576−4580.

(74) O'Connor, N. J.; Jonayat, A. S. M.; Janik, M. J.; Senftle, T. P. Interaction trends between single metal atoms and oxide supports identified with density functional theory and statistical learning. *Nat. Catal.* **2018**, *1*, 531−539.

(75) Campbell, C. T. Energies of Adsorbed Catalytic Intermediates on Transition Metal Surfaces: Calorimetric Measurements and Benchmarks for Theory. *Acc. Chem. Res.* **2019**, *52*, 984−993.

(76) James, T. E.; Hemmingson, S. L.; Campbell, C. T. Energy of Supported Metal Catalysts: From Single Atoms to Large Metal Nanoparticles. *ACS Catal.* **2015**, *5*, 5673−5678.

(77) Mao, Z.; Lustemberg, P. G.; Rumptz, J. R.; Ganduglia-Pirovano, M. V.; Campbell, C. T. Ni Nanoparticles on $CeO_2(111)$: Energetics, Electron Transfer, and Structure by Ni Adsorption Calorimetry, Spectroscopies, and Density Functional Theory. *ACS Catal.* **2020**, *10*, 5101−5114.

(78) Hemmingson, S. L.; James, T. E.; Feeley, G. M.; Tilson, A. M.; Campbell, C. T. Adsorption and Adhesion of Au on Reduced $CeO_2(111)$ Surfaces at 300 and 100 K. *J. Phys. Chem. C* **2016**, *120*, 12113−12124.